Supplementary Materials: Clinical, genomic, and pharmacological study of *MYCN*-amplified *RB1* wild-type metastatic retinoblastoma

Santiago Zugbi, Bsc[1,2†], Daiana Ganiewich, BEng[1,3,†], Arpita Bhattacharyya, MD[4], Rosario Aschero, Bsc[1,2], Daniela Ottaviani, PhD[5], Claudia Sampor, MD[6], Eduardo G. Cafferata, PhD[2,3], Marcela Mena, PhD[1], Mariana Sgroi, MD[7], Ursula Winter, PhD[8], Gabriela Lamas, MD[8], Mariona Suñol, MD[9], Manuel Daroqui, Bsc[10], Edgardo Baialardo, Bsc[10], Beatriz Salas, MD[11], Anirban Das, MD[4], Adriana Fandiño, MD[7], Jasmine H. Francis, MD[12], Fabiana Lubieniecki MD[8], Cinzia Lavarino, PhD[13,14], Ralph Garippa, PhD[15], Osvaldo L. Podhajcer, PhD[2,3], David H. Abramson, MD[12], François Radvanyi, PhD[5], Guillermo Chantada MD, PhD[1,2,14], Andrea S. Llera, PhD[2,3‡], Paula Schaiquevich, PhD[1,2‡*].

Supplementary materials index:

1. Supplementary Methods

1.1. Fluorescent in situ hybridization

For Patient 1, *MYCN* gene amplification was assessed by FISH using a two-color probe that targets *MYCN* (2.24, red signal) and AFF3 (2q1, green signal) used as a reference (Leica Biosystemcs), and for Patient 2, the DNA probe Vysis LSI N-MYC (2p24) SpectrumOrange probe (Abbott) was used. *MYCN* amplification was considered in specimens that exhibited at least 10% of tumor cells with more than eight signals for the MYCN probe and a ration of more than 4 with respect to the reference.

1.2. Bioinformatic analysis

Bioinformatic analysis of raw files obtained from whole exome sequencing in an Illumina HiSeq 4000 instrument consisted of adapter trimming with Cutadapt (v1.18) [70], alignment to GRCh38 using BWA-MEM (v0.7.17) [71], sorting and indexing with Samtools (v1.3.1) and duplicates removal with Picard v2.21.2 [72]. The Genome Analysis Tool Kit (GATK) (v4.1.3.0) was used for germline (HaplotypeCaller) [73] and somatic (Mutect2) variant calling [74], according to their best practices. Called variants were annotated using PeCanPIE [75]. Coverage within the targeted region and the variants was reviewed manually in the BAM files using Integrative Genomics Viewer (IGV) [76], and Alamut Software Suite v.2.14 (Interactive Biosoftware) for variant analysis. Variants with a minor allele frequency (MAF) <0.01 in the population database gnomAD (v2.1.1) [77] and variant allele frequency (VAF) >= 0.05 were selected and checked against ClinVar [12], COSMIC [78], UniProt [79], and GeneCards databases [80], and using the in silico predictors SIFT [81], PolyPhen-2 [82], Mutation Taster-2 [83] and Human Splicing Finder v.3.1 [84]. Variants were listed if they were not classified as benign in databases and predicted to be damaging by at least two predictors. Analysis pipeline was structured using Common Workflow Language [85].

1.3. Western blot and immunoprecipitation

For each cell line, $2x10^6$ cells were harvested and washed twice with ice-cold phosphate-buffered saline. Cells were lysed with buffer (150 mMNaCl, 10 mM Tris-HCl pH 7.4, 1mM EDTA, 1mM EGTA pH 8, 0.2 PMSF, 1% Triton X-100, 0.5% NP-40) supplemented with phosphatase and protease inhibitors. Total protein content was quantified with the Bio-Rad protein assay (Bio-Rad). From each sample, 50μg of protein lysate were used to run western blots with 10% SDS-polyacrylamide gel and transferred to a nitrocellulose membrane (Thermo Scientific). Antibodies used were total pRb mouse antibody (Leica Biosystems, NCL-L.RB358) that recognizes the N-terminal region of the *RB1* gene protein (pRb) and actin rabbit antibody (Sigma, A2066). Western blots were incubated with primary antibodies at 4°C overnight, then with secondary antibodies, either anti mouse IgG or anti-rabbit IgG HRP-linked

(Jackson 111-035-144), and developed with ECL prime western blotting detection kit (Amersham Pharmacia Biotech).

For inmunoprecipitation analysis 200 μg protein extract was incubated with 25μl Protein G Magnetic Beads (BioLabs) at 4°C for 1h to pre-clears crude cell extract of proteins which can bind non-specifically to the beads. Protein extract was incubated with 2 μg of total pRb mouse antibody (Leica Biosystems, NCL-L.RB358) and incubated for 1h at 4°C. Then, 25μl of Protein G Magnetic Beads were added and incubated. The beads were washed two times with Inmunoprecipitation Buffer and beads pellet was resuspended in Sample Loading Buffer. Western blot analysis was performed on a 10% SDS-polyacrylamide gel. After electrophoresis, proteins were transferred to a nitrocellulose membrane (Thermo Scientific). The membrane was blocked with 5% fat-free milk in TBS-T (10mM Tris-HCl pH 7, 150mM NaCl, 1% Tween 20) and incubated with primary mouse antibody against E2F-1 (Santa Cruz Biotechnology, sc-56662). After incubation with secondary antibodies, proteins were visualized with ECL prime western blotting detection kit (Amersham Pharmacia Biotech). In all cases, signal bands were detected on ImageQuant las-4000.

1.4. Large-scale drug High-throughput screening

Tumor cells were seeded in 384-well-plates at 2,000 cells per well in 45 μL of culture media using Multidrop liquid dispenser and exposed to 2,700 bioactive compounds from two drug libraries (Selleck FDA-approved and Selleck Bioactive). Compounds were dissolved in 0.5% DMSO (v/v), added to plates using a Multidrop liquid dispenser at a well concentration of 4.8 μM, and after 72h of drug exposure cell viability was determined. All plates included high (0.5% DMSO) and low controls (100μM melphalan, IC90).

Z' factor and other relevant statistical parameters were calculated [86]. Reproducibility of the screening was evaluated using Y79 cells that were tested in two different days and the cytotoxicity obtained for each compound was compared between occasions.

In all cases, cell viability was determined using CellTiter-Glo® (Promega, Madison, WI) and a Viewlux plate reader (PerkinElmer). Percentage of cell growth was calculated after normalizing luminescence data by logarithmic transformation according to the following equation: % cell growth inhibition = 100* [1-(sample result – high control mean) / (low control mean – high control mean))].

Dose-response curves consisted of 10 to 12 points in the range of 0.03nM to 9.6μM and three independent assays were performed. Each set of data was fitted to four parameter dose response curves using GraphPad Prism v.8 (GraphPad Software Inc, La Jolla, CA) and the calculated parameters included: hill slope, top, bottom, IC50/ EC50 (concentration of each compound that caused a 50% decrease in cell proliferation) and AUC (area under the curve).

Then, drug combination analysis was evaluated in a subset of compounds that showed: published synergistic effects in preclinical models of pediatric oncology, and IC50s that may be clinically achievable based on pharmacokinetic studies reported

elsewhere. Briefly, cells were manually treated in 96-well plates with different drug combinations corresponding to the EC10, EC50, and EC90 of each selected compound in a 3x3 block matrix for each pair of compounds [87]. Each combination of specific concentrations was tested in triplicates and in two independent assays. Cells were incubated with each drug combination for 72h and thereafter viability was assessed with MTT (Sigma-Aldrich) as reported elsewhere [29,69]. Combinations that showed a decrease in cell viability higher than 30% compared to the activity exerted by the single agent were further studied in a full concentration-dose response curve. If so, cells were counted with a hemocytometer, seeded at a density of 10,000 cell per well in triplicates in 96-well plated and cultured for 24 h. Finally, cells were exposed to ten increasing concentrations of compound A and a fixed concentration of compound B (EC25 or EC50). To identify individual dose combinations that were synergistic, we calculated the Combination Index using an open source software program (CompuSyn) [88]. A combination index <1 was considered a synergistic effect [89].

1.5. Establishment and characterization of tumor dissemination of patient-derived xenografts

Under general (100 mg/kg ketamine, 10 mg/kg xylazine) and local (0.5% proparacaine hydrochloride ophthalmic solution) anesthesia, 2 x 10^5 tumor cells resuspended in 2 μL matrigel (BD Bioscience) were injected into the posterior segment of the eyes of 6-week old athymic nude mice (BALBcnu/nu, n=10 per group) as extensively described by Pascual-Pasto G., et al [29]. Injections were performed using a stereomicroscope (M80, Leica microsystems) and when finished, an ointment with erythromycin was used to avoid drying of the eyes until animal recovery and potential infections. Mice were monitored on daily basis for macroscopic ocular tumor growth. Ocular and general clinical state of the animals were recorded including ocular damage associated with the procedure (lens damage, corneal inflammation, uveitis), tumor growth, and signs of tumor disseminated disease (hair loss, abnormal locomotion, weight loss) were recorded. We defined four stages according to the ocular tumor progression being stage 0 the normal mouse eye, stages 1 and 2 when leukocoria could be distinguished and the eye showed proptosis, and stage 3 was defined as an eye with 3-fold the normal size and the experimental endpoint. When eyes reached stage 3, animals were anesthetized and peripheral blood and cerebrospinal fluid from the cisterna magna were collected before being sacrificed. Afterwards, animals were bilaterally enucleated, optic nerves were dissected apart from the ocular globes that were formalin-fixed and paraffin embedded for histopathological examination. The brain, cervical and axillar lymph nodes, and bone marrow specimens were collected, snap frozen and stored at -800°C. To quantify for human retinoblastoma cell dissemination in the tissues of the PDXs, mRNA of the photoreceptor marker CRX was quantified by RT-qPCR using a 7500 Sequence Detection System (Applied Biosystems, Foster city, CA, USA) as previously detailed [16,29]. Briefly, total RNA was isolated using TRIzol (Life Technologies) following the manufacturer's instructions and quantitated using

NanoDrop spectrophotometer. Then, RNA was reverse-transcribed into cDNA using random primers and the SuperScript III kit (Invitrogen). The sequences of primers and probes were previously described [29].

1.6. In vivo efficacy studies in a patient-derived model of lymph node dissemination

First, we examined the tolerability to the concomitant administration of carboplatin, panobinostat and bortesomib in a small group (n=3) non-tumor bearing athymic nude mice. Carboplatin was reconstituted in sterile water, panobinostat and bortezomib in 2% DMSO-98% sterile normal saline, and 1% DMSO-99% sterile water respectively.

Drug combinations and schedule of treatment were designed to mimic potential clinical translation to retinoblastoma [19,20]. Mice were subjected to 2 cycles of chemotherapy of 14 days per cycle. The treatment groups consisted of 6 animals and treatment schemes were as follows: scheme #1: carboplatin at 80 mg/kg, i.p on day 1; 10 mg/kg i.p panobinostat on days 1, 3 and 5; bortezomib 1mg/kg i.v on days 2 and 5. For scheme #2: carboplatin 34 mg/kg i.p on day 1; panobinostat 10 mg/kg i.p on days 1 and 5; bortezomib 1 mg/kg i.v on days 2 and 6. Mouse weight and any possible adverse effect were monitored for each treatment group throughout therapy.

Due to the sudden loss of animal weight and death within the first week of treatment of the 3 animals included in scheme #1, we decided to use scheme #2 in which no animal showed evidence of toxicity.. The weight loss observed in this group was transient and corresponded only to the days after chemotherapy administration.

For efficacy studies, scheme #2 of treatment was evaluated against standard treatment and animals only treated with the vehicle used for dissolving the agents in the PDX model of lymph node dissemination. After 7 days of the intravitreal inoculation of tumor cells, the animals (n=10) were randomized to receive scheme 2 or standard carboplatin therapy. The end point was established as stage 3 of ocular tumor growth or if an eye survival was greater than 100 days after completion of the treatment schedule. In all cases mice were routinely monitored. Disease response was evaluated according to the eye stage.

Statistical comparison between survival curves was performed by log-rank test set at $p<0.05$ as significant.

2. Supplementary Figures

Supplementary Figure S1

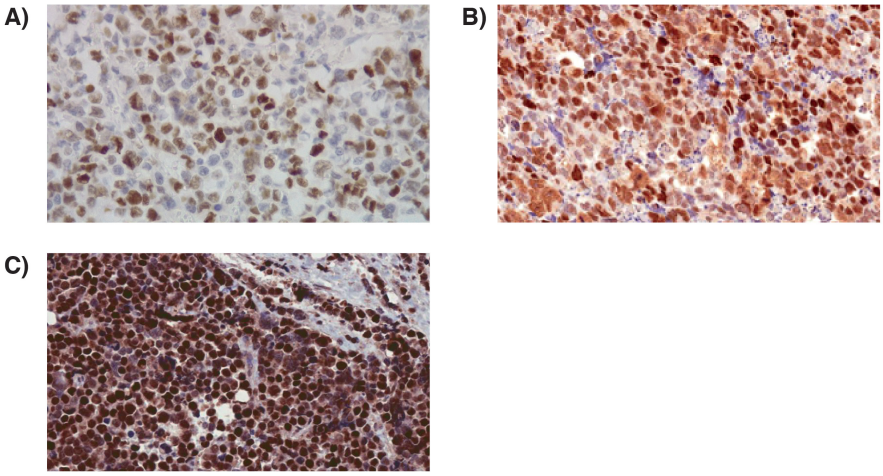

Figure S1. p53 staining of tumor samples from patients
(A) Positive p53 staining in the orbital tumor of Patient 1 and in the **(B)** orbital tumor and **(C)** lymph node specimens of Patient 2. Original magnification 20x.

Supplementary Figure S2

Patient 1 ocular tumor

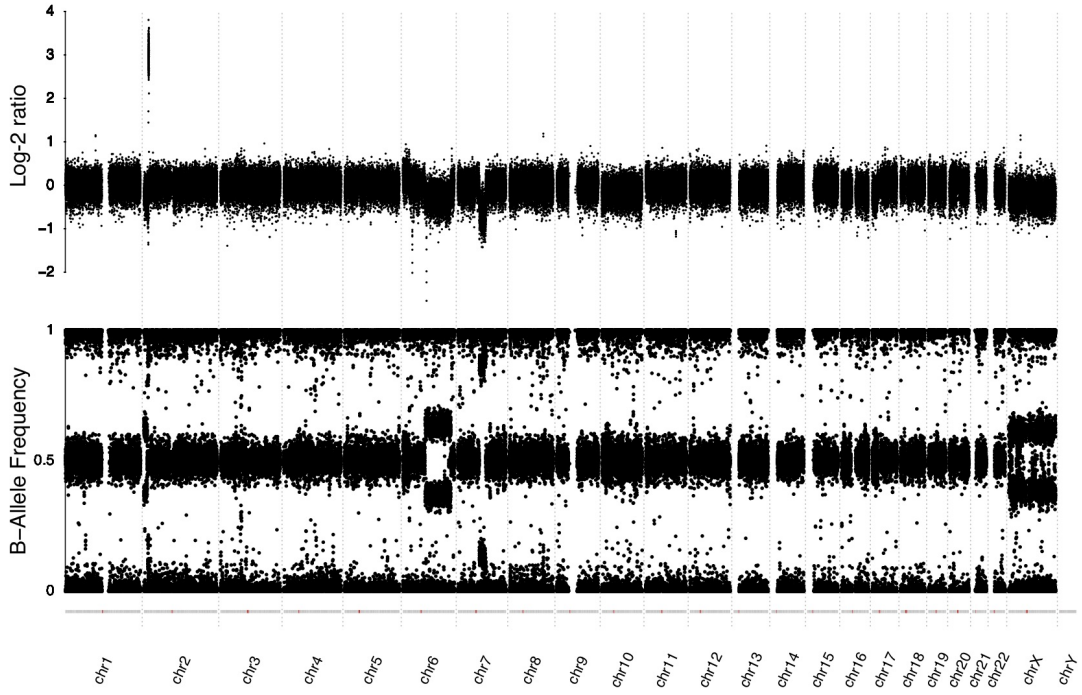

Figure S2. Copy number profile of Patient 1 ocular tumor
Analysis was performed using Oncoscan data. Log-2 relative ratio (upper panel) and B-allele frequency (lower panel) is depicted for all chromosomes.

Supplementary Figure S3

Patient 2 primary ocular tumor (PT)

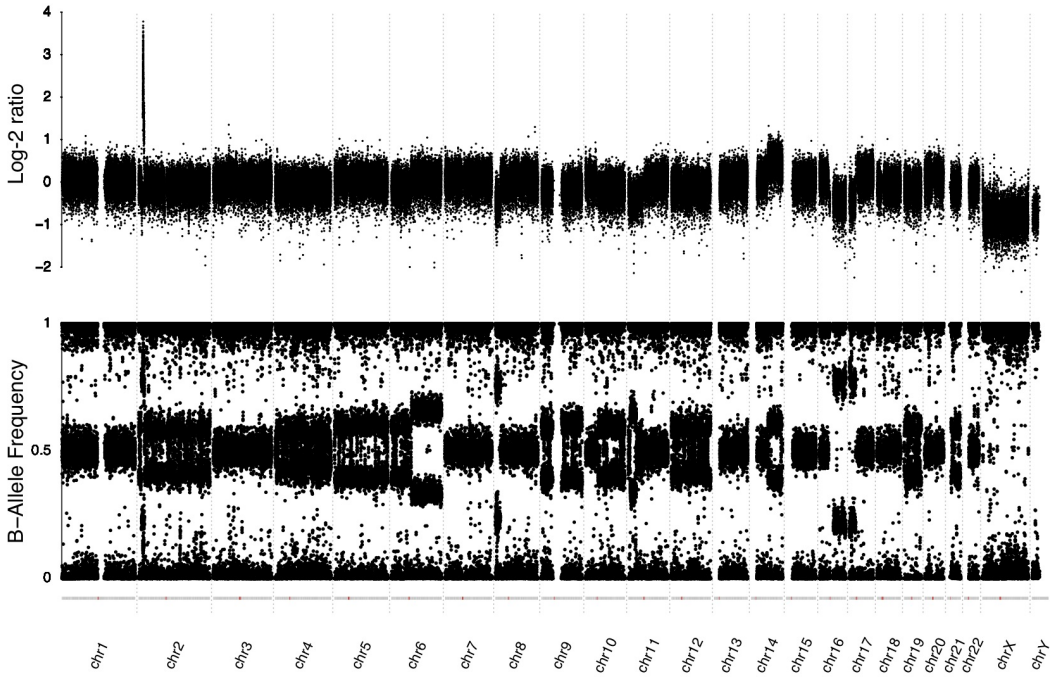

Figure S3. Copy number profile of Patient 2 ocular tumor

Analysis was performed using Oncoscan data. Log-2 relative ratio (upper panel) and B-allele frequency (lower panel) is depicted for all chromosomes.

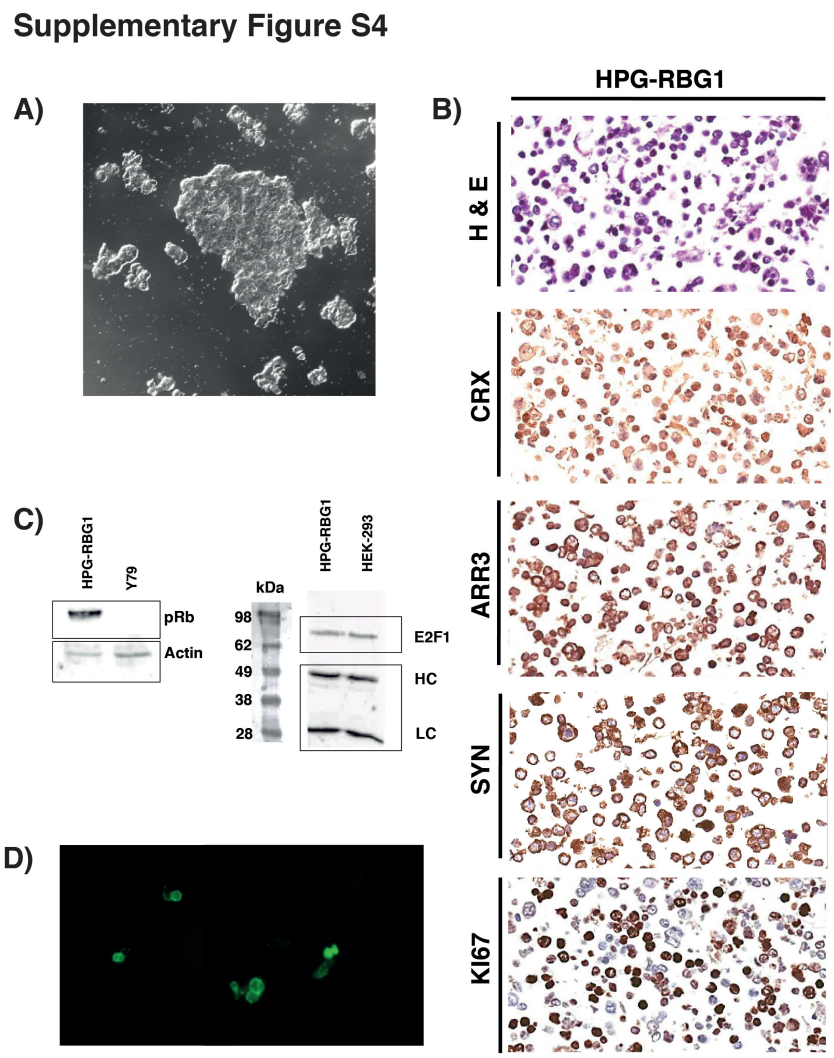

Figure S4. Characterization of HPG-RBG1 cells

(A) Representative confocal microscope image of primary cell culture derived from lymph node dissemination showing cell growth as tumorspheres. **(B)** Hematoxylin and eosin stain shows pleomorphic cells with large and hyperchromatic nucleous that also mark positive for cone-rod homebox (CRX), arrestin3 (ARR3), synapthophysin (SYN), and Ki-67. Original magnification 20x. **(C)** Western blot for retinoblastoma protein (pRb) of HPG-RBG1 cells lysate to validate pRb expression. Co-immunoproceipitation of pRb with E2F1 depicts functional pRb. The relative position for molecular weights (in KDa) are indicated on the right. LC: IgG light chain; HC, IgG heavy chain. **(D)** GD2 positive HPG-RBG1 cells (green fluorescence).

Supplementary Figure S5

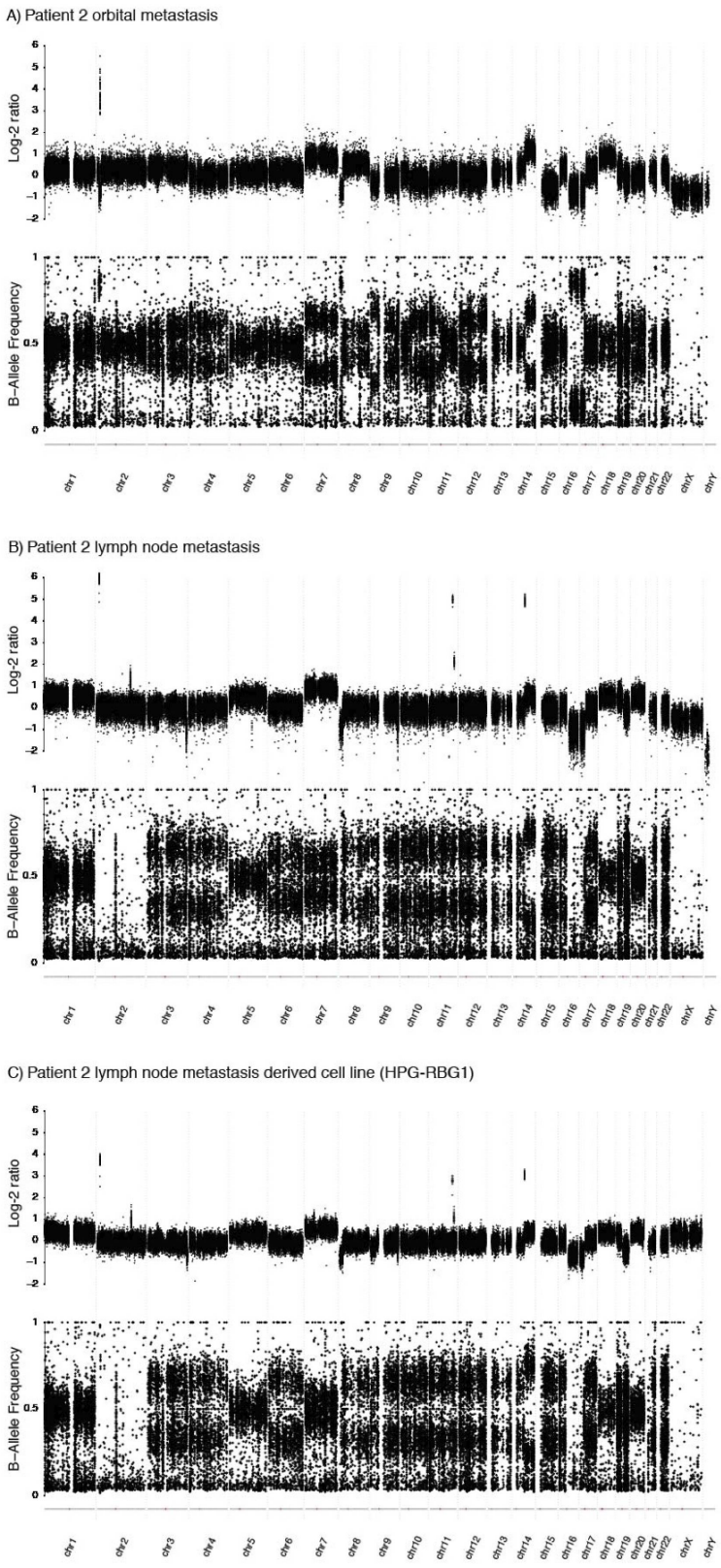

Figure S5. Copy number profiles of patient 2 orbital and lymph node metastasis, and its derived cell line (HPG-RBG1)

Analysis was performed using WES data. Log-2 relative ratio (upper panel) and B-allele frequency (lower panel) is depicted for all chromosomes for **(A)** Patient 2 orbital metastasis, **(B)** Patient 2 lymph node metastasis and **(C)** Patient 2 lymph node metastasis derived cell line (HPG-RBG1).

Supplementary Figure S6

A)

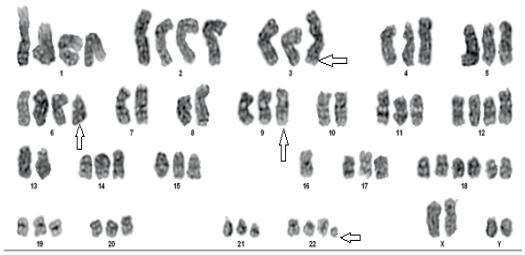

72<2n>, XY, +X, +Y, +1, +1, +2, +2, +add(3)(q27), +4, +5, +6, +?i(6)(p10), +9, ?t(9;22)(q34;q11), +11, +12, +12, +14, +15 ,-16, +17, +18, +18, +18, +18, +19, +20, +21, +22, +22

B)

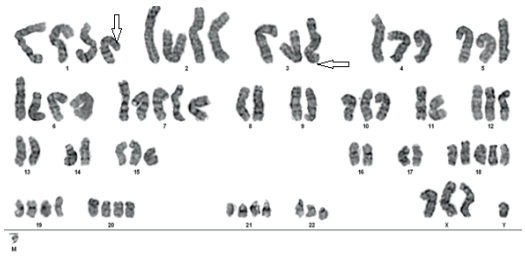

74<2n>, XY, +X, +X, +1, +add(1)(p34), +2, +2, +add(3)(q27), +4, +5, +6, +6, +7, +7, +7, +10, +12, +15, +18, +18, +18, +19, +19, +20, +20, +21, +21, +22, +dmin

C)

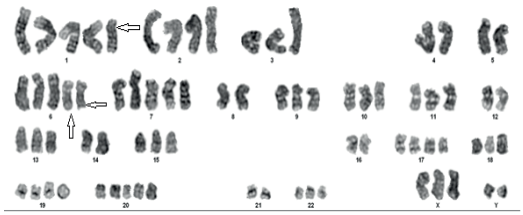

75<2n>, XY, +X, +X, +Y, +1, +1, +del(1)(p34), +2, +2, +3, +6, +del(6)(q?), +del(6)(q?), +7, +7, +7, +9, +10, +11, +13, +15, +17, +17, +18, +19, +der(19), +20, +20, +20, +22

D)

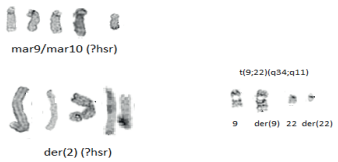

Composite kayrotype

61-76<2n>, XY, +X[7], +X, +X[9], +Y[2], +1[5], +1, +1[9], +1, +1, +1, +1[2], der(1)[3], del(1)(p34)[3], +2[1], +2, +2[6], der(2)?(hsr)[6], +3[6], +3, +3[2], add(3)(q27)[4], +4[9], +5[8], +5, +5[2]. +6[7], +6, +6[3], +del(6)(q?)[2], +del(6)(q?)x2[2], +i(6)(p10)[2], +7[2], +7, +7[7], +7, +7, +7[5], +8[8], +9[7], +9, +9[2], ?t(9;22)(q34;q11)[5], +10[6], +10, +10[2], +11[8], +11, +11[3], +12[6], +12, +12[4], +13[6], +14[5], +15[10], +16[4], +17[9], +17, +17[4], +18[9], +18, +18[2], 19[6], +19, +19[2], +20[3], +20, +20[7], +21[8], +21, +21[5], +22[11], +22, +22[4], +mar1-8, 11-23, +mar9(?hsr)[3], +mar10(?hsr)[2]+dmin[3]{cp18}

Figure S6. Karyotype analysis of HPG-RBG1 lymph node-derived $MYCN_{ampl}$ $RB1^{+/+}$ cell line. **(A)**, **(B)** and **(C)**, representative metaphases of 3 of the 18 cells analyzed, showing the most usual features detected. **(D)**, summary of special features such as double minute and homologous staining regions. **(E)**, composite karyotype description. Arrows indicate chromosomes with structural rearrangement

Supplementary Figure S7

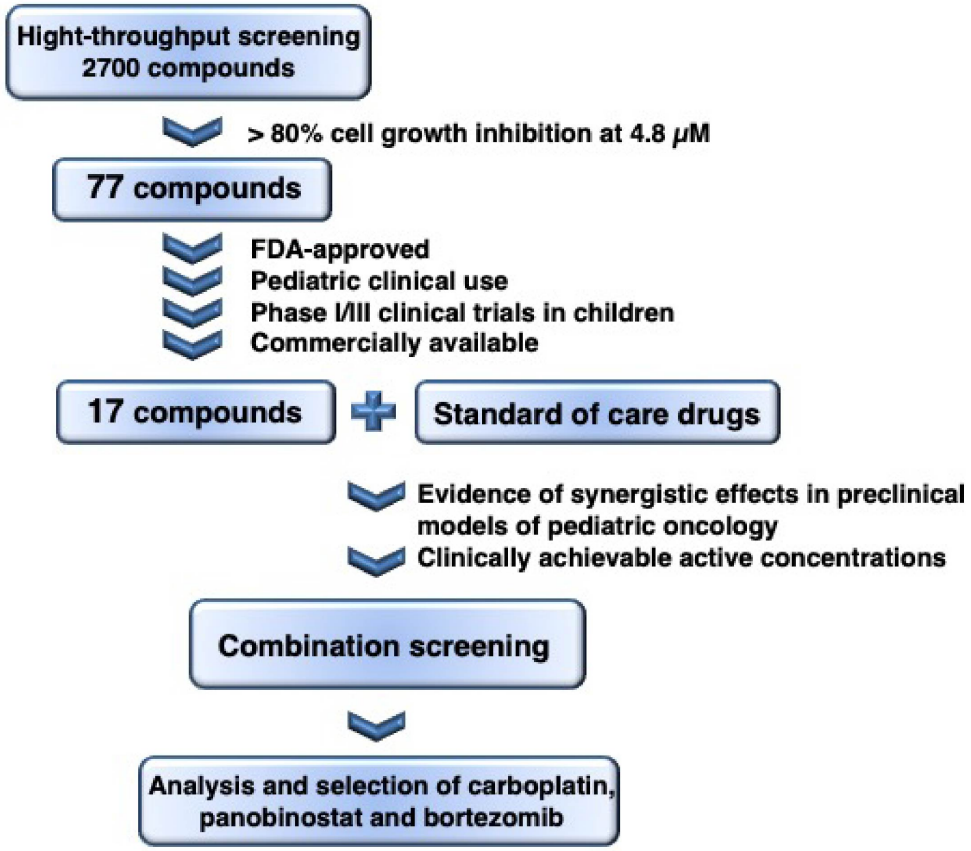

Figure S7. Flowchart depicting the decision selection criteria for drug screening

References

70. Martin, M. Cutadapt removes adapter sequences from high-throughput sequencing reads. *EMBnet.journal* **2011**, *17*, 10. doi:10.14806/ej.17.1.200.

71. Li, H.; Durbin, R. Fast and accurate short read alignment with Burrows-Wheeler transform. *Bioinformatics* **2009**, *25*, 1754–1760.

72. Broad Institute. *Picard Tools*. http://broadinstitute.github.io/picard, accessed 8 June, 2020.

73. Poplin, R.; Ruano-Rubio, V.; DePristo, M.A.; Fennell, T.J.; Carneiro, M.O.; Van der Auwera, G.A.; Kling, D.E.; Gauthier, L.D.; Levy-Moonshine, A.; Roazen, D. et al. Scaling accurate genetic variant discovery to tens of thousands of samples. *bioRxiv* **2018**. doi:10.1101/201178.

74. Van der Auwera, G.A.; Carneiro, M.O.; Hartl, C.; Poplin, R.; Del Angel, G.; Levy-Moonshine, A.; Jordan, T.; Shakir, K.; Roazen, D.; Thibault, J. et al. From FastQ data to high confidence variant calls: the Genome Analysis Toolkit best practices pipeline. *Curr Protoc Bioinformatics* **2013**, *43*, 1–11.

75. Edmonson, M.N.; Patel, A.N.; Hedges, D.J.; Wang, Z.; Rampersaud, E.; Kesserwan, C.A.; Zhou, X.; Liu, Y.; Newman, S.; Rusch, M.C. et al. Pediatric cancer variant pathogenicity information exchange (PECANPIE): A cloud-based platform for curating and classifying germline variants. *Genome Research* **2019**, *29*, 1555–1565. doi:10.1101/gr.250357.119.

76. Robinson, J.T.; Thorvaldsdottir, H.; Winckler, W.; Guttman, M.; Lander, E.S.; Getz, G.; Mesirov, J.P. Integrative genomics viewer. *Nat. Biotechnol.* **2011**, *29*, 24–26.

77. Karczewski, K.J.; Francioli, L.C.; Tiao, G.; Cummings, B.B.; Alfoldi, J.; Wang, Q.; Collins, R.L.; Laricchia, K.M.; Ganna, A.; Birnbaum, D.P. et al. The mutational constraint spectrum quantified from variation in 141,456 humans. *Nature* **2020**, *581*, 434–443.

78. Tate, J.G.; Bamford, S.; Jubb, H.C.; Sondka, Z.; Beare, D.M.; Bindal, N.; Boutselakis, H.; Cole, C.G.; Creatore, C.; Dawson, E. et al. COSMIC: the Catalogue Of Somatic Mutations In Cancer. *Nucleic Acids Res.* **2019**, *47*, D941–D947. https://cancer.sanger.ac.uk/cosmic/.

79. The Uniprot Consortium. UniProt: a worldwide hub of protein knowledge. *Nucleic Acids Res.* **2019**, *47*, D506–D515.

80. Stelzer, G.; Rosen, N.; Plaschkes, I.; Zimmerman, S.; Twik, M.; Fishilevich, S.; Stein, T.I.; Nudel, R.; Lieder, I.; Mazor, Y. et al. The GeneCards Suite: From Gene Data Mining to Disease Genome Sequence Analyses. *Current protocols in bioinformatics* **2016**, *54*, 1.30.1–1.30.33. doi:10.1002/cpbi.5.

81. Vaser, R.; Adusumalli, S.; Leng, S.N.; Sikic, M.; Ng, P.C. SIFT missense predictions for genomes. *Nat Protoc* **2016**, *11*, 1–9.

82. Adzhubei, I.A.; Schmidt, S.; Peshkin, L.; Ramensky, V.E.; Gerasimova, A.; Bork, P.; Kondrashov, A.S.; Sunyaev, S.R. A method and server for predicting damaging missense mutations. *Nat. Methods* **2010**, *7*, 248–249.

83. Schwarz, J.M.; Cooper, D.N.; Schuelke, M.; Seelow, D. MutationTaster2: mutation prediction for the deep-sequencing age. *Nat. Methods* **2014**, *11*, 361–362.

84. Desmet, F.O.; Hamroun, D.; Lalande, M.; Collod-Beroud, G.; Claustres, M.; Beroud, C. Human Splicing Finder: an online bioinformatics tool to predict splicing signals. *Nucleic Acids Res.* **2009**, *37*, e67.

85. Amstutz, P.; Chapman, B.; Chilton, J.; Heuer, M.; Stojanovic, .. Common Workflow Language, v1.0 Common Workflow Language (CWL) Command Line Tool Description, v1.0 **2016**. doi:10.6084/m9.figshare.3115156.v2.

86. Zhang, J.H.; Chung, T.D.; Oldenburg, K.R. A simple statistical parameter for use in evaluation and validation of high throughput screening assays. *Journal of Biomolecular Screening* **1999**, *4*, 67–73. doi:10.1177/108705719900400206.

87. Holbeck, S.L.; Camalier, R.; Crowell, J.A.; Govindharajulu, J.P.; Hollingshead, M.; Anderson, L.W.; Polley, E.; Rubinstein, L.; Srivastava, A.; Wilsker, D. et al. The National Cancer Institute ALMANAC: A

comprehensive screening resource for the detection of anticancer drug pairs with enhanced therapeutic activity. *Cancer Research* **2017**, *77*, 3564–3576. doi:10.1158/0008-5472.CAN-17-0489.

88. Welcome to COMPUSYN. http://www.combosyn.com/. Accessed: 8 June 2020.

89. Chou, T.C. Theoretical basis, experimental design, and computerized simulation of synergism and antagonism in drug combination studies, 2006. doi:10.1124/pr.58.3.10.